

## Highlights

### **H2SGEMM: Emulating FP32 GEMM on Ascend NPUs using FP16 Units with Precision Recovery and Cache-Aware Optimization**

Weicheng Xue, Baisong Xu, Kai Yang, Yongxiang Liu, Dengdeng Fan, Pengxiang Xu, Yonghong Tian

- Emulate FP32 GEMM using FP16-only matrix engines with high precision
- Tunable scaling and decomposition strategy to preserve up to 22-bit mantissa
- Term-wise accumulation improves numerical stability in low-exponent regimes
- Cache-aware blocking and pipelining achieves 77% of peak performance

# H2SGEMM: Emulating FP32 GEMM on Ascend NPUs using FP16 Units with Precision Recovery and Cache-Aware Optimization

Weicheng Xue<sup>a,1</sup>, Baisong Xu<sup>a,1</sup>, Kai Yang<sup>a,1</sup>, Yongxiang Liu<sup>a</sup>, Dengdeng Fan<sup>a</sup>, Pengxiang Xu<sup>a,\*</sup>, Yonghong Tian<sup>a,\*</sup>

*<sup>a</sup>Pengcheng Laboratory, 6001 Shahe West Road,  
Shibilong, Shenzhen, 518055, Guangdong, China*

---

## Abstract

Low-precision matrix engines, such as FP16 cube, offer high throughput but lack support for full-precision computation. In this work, we propose H2SGEMM, a high-performance algorithm for emulating FP32 general matrix-matrix multiplication (GEMM) using only FP16 computation units on a representative AI accelerator. The method decomposes each FP32 operand into two FP16 values and compensates for numerical errors through a tunable scaling strategy. A detailed analysis of numerical errors, including under-flow conditions and precision loss, guides the selection of scaling parameters to preserve up to 22 bits of mantissa accuracy. We further investigate the effect of computation order on accuracy and demonstrate that a term-wise accumulation scheme improves numerical stability over conventional FP32 GEMM in low-exponent regimes. Finally, a cache-aware blocking strategy and double-buffered pipeline are introduced to overlap memory transfers with computation, enabling H2SGEMM to achieve up to 77% of the theoretical FP32-equivalent peak performance on Ascend 910A NPU lacking native FP32 support. Extensive numerical experiments confirm that our method not only recovers the accuracy of native FP32 GEMM but also exhibits superior numerical stability under certain conditions, due to its structured and error-aware computation order.

---

\*Corresponding authors: Pengxiang Xu (xupx@pcl.ac.cn), Yonghong Tian (tianyh@pcl.ac.cn).

<sup>1</sup>These authors contributed equally to this work.

*Keywords:* FP32 emulation, FP16 cube, numerical stability, matrix decomposition, high-performance computing, mixed precision

---

## 1. Introduction

The evolution of specialized accelerators is reshaping the landscape of high-performance computing (HPC). Driven by the rapid progress in deep learning, modern computer systems increasingly rely on heterogeneous architectures that integrate domain-specific hardware. Processors such as NVIDIA GPUs with Tensor Cores, Google’s TPUs, and emerging Neural Processing Units (NPUs) deliver significant speedups for matrix-dominated workloads, offering orders of magnitude higher throughput than traditional CPUs.

These accelerators achieve high performance by concentrating their compute resources on low-precision formats such as half-precision floating point (FP16), bfloat16 (BF16), and INT8. While these formats are sufficient for many machine learning tasks, they are often inadequate for deep learning, scientific and engineering applications [1, 2, 3, 4, 5, 6], which demand the accuracy and dynamic range of FP32 or FP64 arithmetic. This mismatch presents a growing challenge: the most powerful computing platforms are optimized for formats that are incompatible with the precision requirements of many established scientific workloads.

To bridge this gap, this work investigates how to efficiently harness the compute density of low-precision hardware for workloads that require FP32-level accuracy. Specifically, we target scenarios where native FP32 matrix multiplication (GEMM) is unsupported or inefficient, such as on Ascend 910A NPUs that expose high-performance FP16 tensor engines but lack equivalent FP32 compute units.

We propose **H2SGEMM**, a software–hardware co-designed framework that enables high-throughput and high-accuracy FP32 GEMM using only FP16 computation. At its core, H2SGEMM combines a numerical emulation technique with a performance-optimized implementation tailored to the memory hierarchy of a representative AI accelerator.

The main contributions of this work are:

- **A general algorithm for FP32 emulation:** We present H2SGEMM, an algorithm that decomposes each FP32 operand into a pair of FP16 values, a high-order component and a residual, and recombines their

products to reconstruct FP32-level results, preserving up to 22 bits of mantissa accuracy.

- **Error analysis and numerical control:** We perform a detailed study of precision loss due to rounding and underflow, and introduce two mitigation strategies: (1) a tunable amplification factor applied to residual terms, and (2) a term-wise accumulation scheme that improves numerical stability over traditional reduction orders.
- **Architecture-aware optimization:** We develop a set of performance strategies including L1-cache-aware tiling and a software-level double-buffered pipeline. These techniques overlap memory movement and computation, effectively hiding the cost of decomposition and enabling high hardware utilization.
- **Empirical validation:** We evaluate H2SGEMM on Ascend 910A, a representative AI accelerator with FP16-only GEMM engines. Results show that H2SGEMM achieves up to 77% of the FP32-equivalent theoretical peak and, in some cases, exceeds the numerical accuracy of native sgemm implementations under low-exponent inputs.

## 2. Background and Related Work

The growing gap between the numerical precision requirements of scientific computing and the capabilities of modern AI-oriented accelerators has prompted renewed interest in mixed-precision algorithms. While many scientific applications still demand FP32 or FP64 precision for numerical stability, contemporary hardware increasingly favors lower-precision formats such as FP16 or even FP8 to maximize throughput and energy efficiency. For example, the FP8 Tensor Core throughput of the NVIDIA H100 is roughly 60 $\times$  higher than its FP64 throughput, and the Ascend 910A NPU [7] delivers  $\sim 256$  TF/s in FP16 but lacks efficient support for FP32 GEMM. These trends highlight both a challenge and an opportunity: *how to emulate high-precision matrix computations using low-precision arithmetic units without compromising accuracy.*

A natural approach to address the precision–performance tradeoff is through mixed-precision techniques. The idea of performing most computations in lower precision and then refining results in higher precision has a long history in numerical linear algebra, particularly in iterative refinement solvers.

These methods rely on selectively using high-precision arithmetic in numerically sensitive operations, while exploiting faster low-precision operations elsewhere to gain performance.

In contrast to such hybrid strategies, recent work has explored a more direct direction: emulating high-precision GEMM (e.g., FP32) using only low-precision hardware such as FP16. Rather than mixing precisions, these methods decompose each high-precision operand into two or more low-precision components, typically capturing the high and low bits of the significand, and reformulate the original matrix product as a sum of multiple low-precision GEMMs. This line of work aims to preserve high numerical accuracy while operating entirely on accelerators that lack efficient FP32 units.

The foundational work by Ozaki et al. [8] formalized this idea by expressing the product of two FP64 matrices as a series of lower-precision GEMMs with a priori error bounds. Although originally targeted at double precision, this decomposition strategy laid the groundwork for FP32-from-FP16 emulation schemes. Markidis et al. [9] were among the first to explore such techniques on GPUs, proposing a two-pass approach based on splitting FP32 inputs into FP16 components. Their method performed an initial FP16 GEMM followed by a corrective residual GEMM. However, their use of round-towards-zero (RZ) conversion introduced a systematic 2-bit precision loss compared to full FP32 accuracy, owing to uncorrected rounding errors in the low-order bits.

To reduce this error, Feng et al. [10] proposed Egemm-TC, a refinement that adopted a more careful decomposition and a rounding strategy closer to round-to-nearest (RN). Their implementation included warp-level cache reuse and register pipeline optimizations, yielding a  $3.13\times$  speedup over cuBLAS FP32 GEMM on NVIDIA Turing GPUs. However, the decomposition still failed to fully account for the implicit leading bit in FP32 representation, limiting the worst-case precision to  $\sim 21$  bits.

Ootomo and Yokota [11] later identified another key source of error: the use of Tensor Cores for accumulation. Tensor Core units perform multiplications in FP16 but may accumulate results using internal FP32 registers with RZ rounding [12]. This caused a bias that could not be corrected by earlier schemes. They proposed performing the residual accumulation outside the Tensor Core, using standard FP32 units with unbiased RN rounding. By scaling intermediate terms to prevent underflow and carefully structuring the summation, their approach achieved bit-for-bit FP32 accuracy on A100 GPUs. Performance-wise, their CUTLASS-based implementation delivered

up to 51 TFLOPS—more than  $2\times$  the peak native FP32 throughput. To support matrices spanning the full FP32 exponent range, they later integrated TensorFloat-32 (TF32) into their framework, attaining  $\sim 33$  TFLOPS with negligible ( $\sim 1$ -bit) precision loss.

Ma et al. [13] further advanced this line of work by introducing an optimized operand decomposition scheme that emulates FP32 precision using only FP16 operations. Their method carefully accounts for the implicit leading bit in the FP32 mantissa, reducing the worst-case error to approximately one bit. To sustain high throughput, they implemented different memory pipeline strategies that overlaps tile loading with computation, ensuring that the Tensor Cores remain fully utilized. Their implementation on NVIDIA A100 achieved 64.15 TFLOPS FP32-equivalent GEMM—approximately 61.7% of the chip’s theoretical FP16 peak—while preserving near-full FP32 accuracy.

Despite these advances, challenges remain. A single FP16 multiplication carries at most  $\sim 11$  bits of precision (including the hidden bit), compared to 24 bits in FP32. Therefore, converting and computing in FP16 inevitably introduces quantization and accumulation errors. Two-pass methods recover much of the lost accuracy, but small residual errors persist unless additional corrective passes are introduced. Accumulating many FP16 products is also nontrivial due to the narrow exponent range of FP16, which can lead to overflow or cancellation errors. Algorithms must carefully structure their summations—e.g., by summing larger terms first or splitting into multiple passes—to preserve significance.

To make such error-reduction techniques practical without sacrificing performance, it is essential to minimize their computational and memory overhead. The most effective methods address this by incorporating system-level optimizations, including tiling and cache-aware buffering strategies, which help hide memory latency and keep low-precision units fully utilized.

In this context, we propose **H2SGEMM**, a novel algorithm for single-precision GEMM emulation on hardware with only FP16 matrix engines. H2SGEMM is designed to combine high numerical accuracy with high sustained throughput on accelerators that lack efficient FP32 support. Its key innovation lies in its unified design: it integrates a numerically accurate decomposition scheme with a system-level pipelining strategy to minimize memory overhead.

Numerically, H2SGEMM splits each FP32 matrix into two FP16 components and performs multiple scaled GEMMs whose products are term-wise

accumulated. This strategy achieves FP32 accuracy. On the system side, H2SGEMM employs cache-aware tiling and double buffering to overlap data movement with computation. Tiles are sized to fit in L1 buffer, and two streams of tiles are maintained in alternating buffers to hide load/store latency. As a result, the additional computation introduced by decomposition does not stall the pipeline, and FP16 units remain fully utilized.

Table 1: Comparison of FP32 emulation methods using FP16 hardware

Work	Hardware Target	Decomposition / Rounding Method	Precision Loss	Error Control Mechanisms	Performance Claim
Markidis et al. [9]	NVIDIA V100	Truncation-based (RZ)	2 bits	Not detailed	Trade-off between performance and precision
Feng et al. [10]	NVIDIA T4 & RTX6000	Decomposition without hidden bit, RZ	2 bits	Warp-level cache/register pipeline optimization	3.13× speedup over cuBLAS FP32
Ootomo et al. [11]	NVIDIA A100	Decomposition with amplification, RN	1 bit	Lacked detailed underflow/rounding error control	51 TFLOPS (surpassing theoretical FP32 peak)
Ma et al. [13]	NVIDIA V100, T4, A100	Optimized decomposition, RN	1 bit	Lacked deep error control design and analysis	64.15 TFLOPS (61.7% of theoretical peak)
<b>This Work (H2SGEMM)</b>	<b>Ascend 910A</b>	<b>Decomposition with tunable amplification, RN</b>	<b>~1 bit</b>	<b>Tunable amplification, Term-wise accumulation</b>	<b>65.3 TFLOPS (77% of theoretical FP32-equivalent peak)</b>

### 3. Methodology

#### 3.1. Floating-Point Decomposition Algorithm

##### 3.1.1. Fundamentals

According to the IEEE-754 floating-point standard [14], a single-precision (FP32) number uses 32 bits, including 1 sign bit, 8 exponent bits, and 23 mantissa bits, along with 1 implicit leading bit. A half-precision (FP16) number uses 16 bits, comprising 1 sign bit, 5 exponent bits, and 10 mantissa bits, also with an implicit leading bit. The standard FP32 format can be expressed by Eq. 1:

$$V = (-1)^S \times 2^{(E-127)} \times 1.M \quad (1)$$

Here,  $S$  is the sign bit,  $E$  is the 8-bit exponent, and  $E - 127$  is the unbiased exponent, denoted as  $E_{\text{offset}}$ .  $M$  is the 23-bit mantissa with an implicit leading 1 before the decimal point.

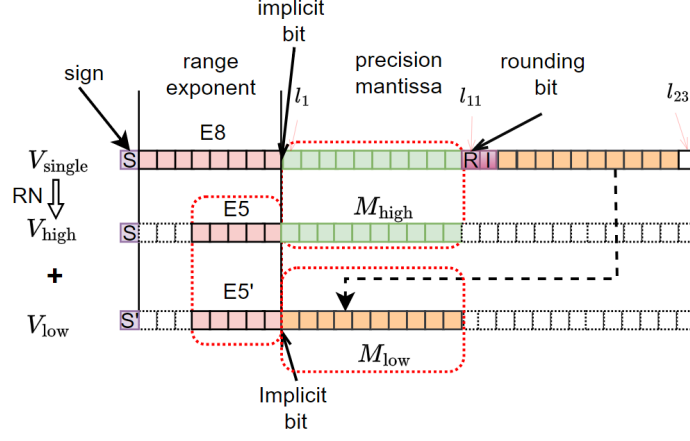


Figure 1: Splitting a single FP32 floating number into two FP16 floating numbers

The FP32 value  $V$  can be decomposed into a high part  $V_{\text{high}}$  and a low part  $V_{\text{low}}$ , as illustrated in Fig. 1. The decomposition follows the round-to-nearest-even (RN) rule. The high part is computed using the leading 10 bits of the mantissa plus the implicit bit, with the 11th bit used for rounding. In most cases, the rounding bit becomes zero after rounding. A special case occurs when the last bit of the high mantissa is zero, the rounding bit is one, and all remaining bits are zero. Hence, the rounding bit is not directly retained in the low part. For the low part, the remaining 13 bits after rounding are used, beginning from the first non-zero bit, and rounded according to RN. The decomposition process is expressed in Eq. 2:

$$\begin{cases} V_{\text{high}} = \begin{cases} (-1)^S \times 2^{(E'-15)} \times 1.M_{\text{high}} & \text{if } 1 \leq E' \leq 30 \text{ (normalized)} \\ (-1)^S \times 2^{-14} \times 0.M_{\text{high}} & \text{if } E' = 0 \text{ (subnormal)} \end{cases} \\ V_{\text{low}} = \begin{cases} (-1)^{S'} \times 2^{(E'-15-11-1-N)} \times 1.M_{\text{low}} & \text{if } 1 \leq (E' - 11 - 1 - N) \leq 30 \\ & \text{(normalized)} \\ (-1)^{S'} \times 2^{-14} \times 0.M_{\text{low}} & \text{if } (E' - 11 - 1 - N) = 0 \\ & \text{(subnormal)} \end{cases} \end{cases} \quad (2)$$

Here,  $E'$  is the 5-bit FP16 exponent, and  $E' - 15$  and  $E' - 12 - N - 15$  represent the offset exponents of the high and low parts.  $R$  denotes the carry introduced by rounding the high part:  $E - 127 + R = E' - 15$ , with  $R = 1$  if rounding carries, otherwise 0. If  $R = 1$ , the low part's sign bit may flip.  $M_{\text{high}}$



and  $M_{\text{low}}$  are the 11-bit mantissas of the high and low parts, respectively.  $N$  is the number of leading zeros in the mantissa of  $V_{\text{low}}$  after truncation, with  $0 \leq N \leq 10$ .

The original FP32 value can be approximately reconstructed by summing the two FP16 components:  $V \approx V_{\text{high}} + V_{\text{low}}$ . This decomposition theoretically preserves at least 22 mantissa bits—one less than FP32 and 11 more than a standalone FP16 representation—enabling accuracy recovery. While it introduces additional computational cost and hardware/software support requirements, it enhances flexibility under hardware precision constraints, usually exist for modern AI chips.

### 3.1.2. Probability of Underflow and Gradual Underflow

Underflow and gradual underflow primarily affect  $V_{\text{low}}$ . Given Ascend processors adopt RN rounding, we categorize probabilities accordingly. Let  $P(N = n, X)$  be the probability of an event  $X$  (truncation  $T$  or rounding  $R$ ) given  $N = n$ :

$$P(N = n, X) = \begin{cases} 0 & \text{if } n < -1 \\ \left(\frac{1}{2}\right)^{l_M - l_{M_{\text{high}}} + 1} & \text{if } n = -1 \text{ and } X = T \text{ or } R \\ \left(\frac{1}{2}\right)^{n+2} & \text{if } 0 \leq n < l_M - l_{M_{\text{high}}} - 1 \text{ and } X = T \text{ or } R \\ \left(\frac{1}{2}\right)^{l_M - l_{M_{\text{high}}}} & \text{if } n = l_M - l_{M_{\text{high}}} - 1 \text{ and } X = T \\ 0 & \text{if } n = l_M - l_{M_{\text{high}}} - 1 \text{ and } X = R \end{cases} \quad (3)$$

Here,  $l_M = 23$  (FP32 mantissa), and  $l_{M_{\text{high}}} = 10$  (FP16 mantissa). The special case  $n = -1$  corresponds to when the 11th mantissa bit is 1 and the remaining bits are 0.

Underflow conditions must satisfy:

$$\begin{cases} E_{\text{offset}} - l_{M_{\text{high}}} + b_{\text{low}} - 3 < N & \text{(gradual underflow)} \\ E_{\text{offset}} + b_{\text{low}} - 3 < N & \text{(underflow)} \end{cases} \quad (4)$$

where  $b_{\text{low}} = 15$  is the FP16 exponent bias. The probabilities are then:

$$\begin{cases} P_{u+gu}(E_{\text{offset}}) = \sum_{N=E_{\text{offset}}-l_{M_{\text{high}}}+b_{\text{low}}-2}^{l_M-l_{M_{\text{high}}}-1} (P(N, T) + P(N, R)) \\ P_u(E_{\text{offset}}) = \sum_{N=E_{\text{offset}}+b_{\text{low}}-2}^{l_M-l_{M_{\text{high}}}-1} (P(N, T) + P(N, R)) \end{cases} \quad (5)$$

As shown in Fig. 2(a), underflow becomes significant when the offset exponent is small. If subnormals are not supported, the probability of gradual underflow exceeds 10% at  $E_{\text{offset}} = 0$ . If subnormals are supported, significant underflow occurs only below  $E_{\text{offset}} = -10$ , approaching 100% at  $E_{\text{offset}} < -12$ .

### 3.1.3. Applicability and Scaling

In practice, users rarely know  $N$  directly. When underflow begins (e.g.,  $N = 10$ ), if  $(E' - 15 - 12 - 10) < -24$ , fewer than 22 bits are preserved. Scaling the low part compensates for this. If complete underflow occurs ( $N = 0$ ) and  $(E' - 15 - 12 - 0) < -24$ , precision collapses to 11 bits. Hence:

**Rule 1:** Under RN rounding, when the absolute value of an FP32 number is below  $2^{-2}$ , the low part must be scaled to preserve 22 bits. If the value is below  $2^{-12}$ , decomposition fails without sufficient scaling.

If the FP32 number is below the FP16 subnormal threshold ( $2^{-24}$ ), both parts must be scaled, which is beyond our current scope.

For the low part, amplification may limit its representable upper bound. Using a scaling factor  $sf = 2^{sb}$ , overflow may occur when the low part reaches its upper range. Setting  $N = 0$ , the offset exponent becomes  $E' - 15 - 12 + sb$ . If this exceeds the FP16 maximum offset exponent (i.e., 15), additional precision loss may result due to overflow. To avoid this, we introduce the following rule:

**Rule 2:** Under RN rounding, if large FP32 values are present, the scaling factor should not exceed  $2^{12}$  to avoid overflow in the lower component.

Rules 1 and 2 jointly define the allowable bounds for the scaling exponent  $sb$ . As expressed in Eq. 6, these bounds ensure that the decomposition algorithm preserves 22 effective mantissa bits from the original FP32 input.

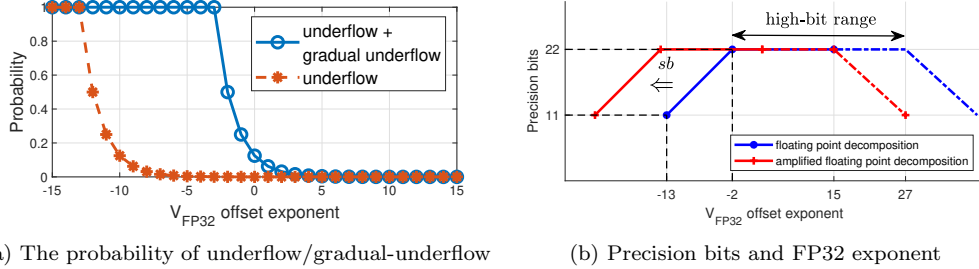


Figure 2: Analysis of FP32 underflow/gradual underflow and precision bits

By selecting an appropriate  $sb$  within this range, the decomposition maintains near-full precision while avoiding both underflow and overflow.

$$-24 + 22 - (E' - 15)_{\min} \leq sb \leq 15 + 12 - (E' - 15)_{\max} \quad (6)$$

The choice of  $sb$  depends on the input data’s dynamic range and required numerical precision. When the input distribution is unknown, a conservative assumption is to treat the values as spanning the entire FP16 representable range, i.e., with offset exponents  $(E' - 15)_{\min} = -14$  and  $(E' - 15)_{\max} = 15$ . Under this assumption, a scaling exponent of  $sb = 12$  is a reasonable and robust choice. In deep learning workloads, where both weights and updates typically have small magnitudes, the upper bound constraint is often negligible. Hence, a scaling factor of  $2^{12}$  remains suitable in practice.

Based on Eq. 6, Fig. 2(b) shows how the number of retained mantissa bits varies with the offset exponent of the original FP32 input, both with and without scaling. Without amplification, precision degrades gradually as the exponent decreases. When applying a scaling exponent of  $sb = 12$ , the curve is effectively shifted left by 12 bits, significantly expanding the high-precision region. In particular, input values with offset exponents in the range  $[15, 27]$ —which cannot be represented in FP16 format—are remapped into the representable range  $[3, 15]$ , thereby maximizing bit retention within the FP16 domain.

### 3.2. Half-to-Single Precision Matrix Multiplication and Error Analysis

Matrix multiplication is a core operation in deep learning. To accelerate computation, low-precision units (e.g., FP16) are often used instead of FP32. However, converting FP32 inputs directly to FP16 reduces precision to 11 bits. To mitigate this, a half-to-single conversion algorithm can be employed, as formulated in Eq. 7:

$$\left\{ \begin{array}{l} A_{\text{half}} = \text{to\_half}(A_{\text{single}}), \quad R_{A,\text{half}} = \text{to\_half}((A_{\text{single}} - \text{to\_single}(A_{\text{half}})) \times sf) \\ B_{\text{half}} = \text{to\_half}(B_{\text{single}}), \quad R_{B,\text{half}} = \text{to\_half}((B_{\text{single}} - \text{to\_single}(B_{\text{half}})) \times sf) \\ C_{\text{single}} = A_{\text{single}} B_{\text{single}} \\ \quad \approx (A_{\text{half}} + R_{A,\text{half}}/sf)(B_{\text{half}} + R_{B,\text{half}}/sf) \\ \quad \approx A_{\text{half}} B_{\text{half}} + B_{\text{half}} R_{A,\text{half}}/sf + A_{\text{half}} R_{B,\text{half}}/sf + \cancel{R_{A,\text{half}} R_{B,\text{half}}/sf^2} \end{array} \right. \quad \begin{array}{l} \mathbf{0} \\ (7) \end{array}$$

Here,  $A_{\text{single}}, B_{\text{single}}$  are FP32 inputs, and  $C_{\text{single}}$  is the FP32 output. The high parts  $A_{\text{half}}, B_{\text{half}}$  and scaled low parts  $R_{A,\text{half}}, R_{B,\text{half}}$  are stored as FP16 values.

This method introduces errors from decomposition, rounding, and accumulation. RN rounding provides higher precision than RZ. The accumulation of intermediate products in matrix multiplication can introduce both under-flow and rounding errors. For example, storing intermediate results in FP32 format rather than lower-precision types helps prevent precision loss. In addition, carefully reordering the accumulation sequence can mitigate rounding error propagation. The final term can typically be omitted due to its negligible contribution.

### 3.3. Implementation

#### 3.3.1. Cache-Aware Blocking

For large-scale input matrices, blocking is essential to reduce memory footprint. The Ascend NPU features a two-level cache hierarchy—L1 and L0 (Fig. 3). Since the memory bandwidth between L1 and main memory is significantly lower than that between L1 and L0, data movement becomes the bottleneck. Consequently, block sizes should be carefully selected to retain operands in the L1 cache as long as possible, minimizing global memory accesses [15].

During matrix multiplication, FP32 inputs are first converted to FP16 and stored in L1 to feed the cube compute unit. Each AI core provides 512 KB of L1 buffer for FP16 data. When computing  $C = A \times B + C$ , the blocking strategy in Fig. 4 is applied, with two primary design principles:

- (1) maximize L1 reuse of matrix  $A$  blocks to increase their residency;
- (2) reserve space in L1 for double buffering of matrix  $B$  blocks to enable alternating access.

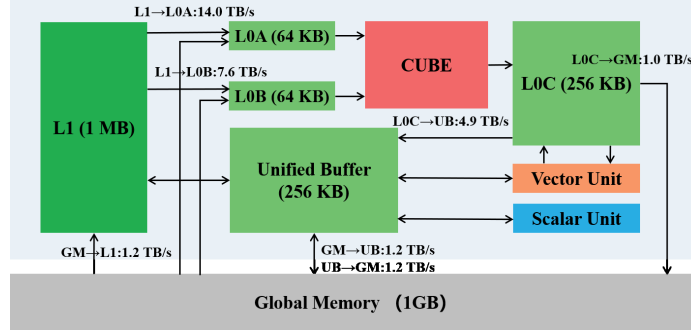


Figure 3: DaVinci architecture of Huawei Ascend NPU AI core

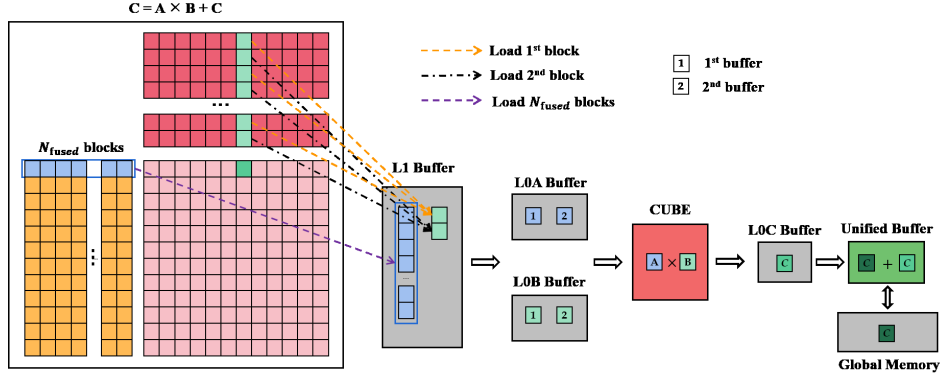


Figure 4: Matrix blocking based on L1 cache reuse

These principles ensure that matrix  $A$  blocks are stored in a row-major fashion within L1. Their count is mainly constrained by L1 capacity. In each fused iteration, matrix  $B$  blocks are streamed column-wise into alternating L1 buffers. The number of fused iterations  $N_{\text{fused}}$ , defined as the number of  $A$  blocks in L1, is calculated as:

$$N_{\text{fused}} = \text{int} \left( \frac{L1 - 2b_k b_n}{b_m b_k} \right) = \text{int} \left( \frac{L1}{b_m b_k} - 2 \frac{b_n}{b_m} \right) = f \frac{L1}{b_m b_k} \quad (8)$$

Here,  $b_m$  and  $b_k$  are the block height and width of matrix  $A$ , and  $b_n$  is the block width of matrix  $B$ . The constant  $f$  reflects the correction from  $\frac{b_n}{b_m} \sim O(1)$  and the floor operation, and depends on L1 size,  $A$  block dimensions, and the  $C$  block aspect ratio. Increasing  $A$  block size reduces  $N_{\text{fused}}$ , and vice versa.

The total memory traffic from main memory to L1 for matrix  $A$  ( $A_r$ ), for

matrix  $B$  ( $B_{\mathbf{r}}$ ), and the read/write volume for  $C$  via the unified buffer (UB) ( $C_{\mathbf{rw}}$ ) is summarized in Eq. 9:

$$\left\{ \begin{array}{l} A_{\mathbf{r}} = b_m b_k M K = m k \\ B_{\mathbf{r}} = b_k b_n K N \frac{m}{N_{\text{core}} b_m} = \frac{m k n}{N_{\text{core}} b_m} \\ C_{\mathbf{rw}} = 2 b_m b_n M N \frac{K}{N_{\text{fused}}} = \frac{2 m k n b_m}{f L 1} \\ \text{data}_{\mathbf{rw}} = A_{\mathbf{r}} + B_{\mathbf{r}} + C_{\mathbf{rw}} = m k + \frac{m k n}{N_{\text{core}} b_m} + \frac{2 m k n b_m}{f L 1} \end{array} \right. \quad (9)$$

Here,  $m$ ,  $k$ , and  $n$  are the dimensions of matrices  $A$  and  $B$ , and  $M$ ,  $K$ , and  $N$  are the number of blocks in each dimension.  $N_{\text{core}} = 32$  denotes the number of AI cores, which parallelize the computation across different  $A$  block rows for a given  $B$  block. Each  $B$  block must be loaded approximately  $\frac{m}{N_{\text{core}} b_m}$  times, and each  $C$  block must be read and written  $\frac{K}{N_{\text{fused}}}$  times.

To ensure correctness and prevent memory overflows in FP16 GEMM, the block dimensions are subject to hardware-imposed constraints (Eq. 10) including cube computation, L0A/L0B APIs, and UB buffer capacity:

$$\left\{ \begin{array}{ll} b_m, b_k, b_n \equiv 0 \pmod{16} & \text{(cube computation constraints)} \\ b_m \times b_k \leq 64 \times 256 & \text{(L0A capacity)} \\ b_k \times b_n \leq 64 \times 256 & \text{(L0B capacity)} \\ b_m \times b_n \times 6 \leq 248 \times 1024 & \text{(L0C and UB capacity)} \end{array} \right. \quad (10)$$

Since the L1–L0 bandwidth is high but L0 capacity is small, we focus only on L1-level blocking and ignore L0 reuse. Eq. 10 does not enforce minimum L0 utilization to keep analysis tractable. With  $\frac{L1}{b_m b_k} \geq 16$ , the fusion degree typically satisfies  $N_{\text{fused}} \sim O(10)$ .

Fig. 5 shows how  $N_{\text{fused}}$  and  $f$  vary with  $b_m b_k$  and  $b_n/b_m$ . In the range  $0.5 \leq b_n/b_m \leq 2$ ,  $N_{\text{fused}}$  is roughly inversely proportional to  $b_m b_k$ , with weak dependence on  $b_n/b_m$ . The fusion efficiency  $f$  remains between 0.92 and 1.0, indicating high L1 utilization. As  $b_m b_k$  increases,  $f$  drops slowly; as  $b_n/b_m$  increases,  $f$  decreases monotonically. Due to Eq. 10 constraints, larger  $b_n/b_m$  values reduce feasible block configurations.

An optimal  $b_m$  can be estimated as  $b_{m,\text{optimal}} = \sqrt{\frac{f L 1}{2 N_{\text{core}}}}$ , which lies in  $86 < b_{m,\text{optimal}} < 90$ . Rounding to the nearest multiple of 16 gives  $b_m = 96$ .

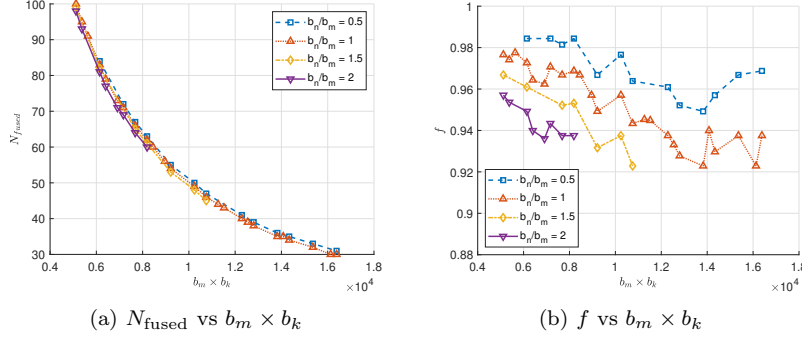


Figure 5: Impact of blocking size on  $N_{\text{fused}}$  and  $f$

This serves as a baseline for performance evaluation and tuning.

### 3.3.2. Double-Buffered Pipelining

Fig. 6 compares two pipeline architectures on Ascend NPUs: (a) a single-buffered pipeline and (b) a double-buffered variant. The double-buffer design aims to overlap memory transfers and computation across L1, L0A, and L0B buffers, improving data availability to the cube compute unit and enhancing performance.

In Fig. 6(a), the single-buffered pipeline incurs strict data dependencies between compute and memory stages. Each compute step waits for full data movement from memory to L1 before proceeding, causing idle cycles in the cube unit and reducing throughput.

In contrast, Fig. 6(b) shows the double-buffered design, which separates read/write channels to overlap computation and memory access. When one buffer feeds the cube with current  $A_{\text{half}}$  and  $B_{\text{half}}$ , the other buffer prefetches the next blocks. Data movement proceeds in four stages: (1)  $B_{\text{single}}$  is loaded into UB, (2) converted to  $B_{\text{half}}$ , (3) transferred to L1, and (4)  $A_{\text{half}}$  and  $B_{\text{half}}$  are moved to L0. If GEMM computation cost is large enough to hide memory latency, all stages can overlap with GEMM. Though more complex, this strategy significantly reduces cube idle time and increases pipeline concurrency.

Eq. 7 shows the half-to-single precision expansion used in GEMM, involving three terms:  $A_{\text{half}}B_{\text{half}}$ ,  $B_{\text{half}}R_{A,\text{half}}/sf$ , and  $A_{\text{half}}R_{B,\text{half}}/sf$ . These terms are similar in structure; for brevity, we detail only the second in Algorithm 1.

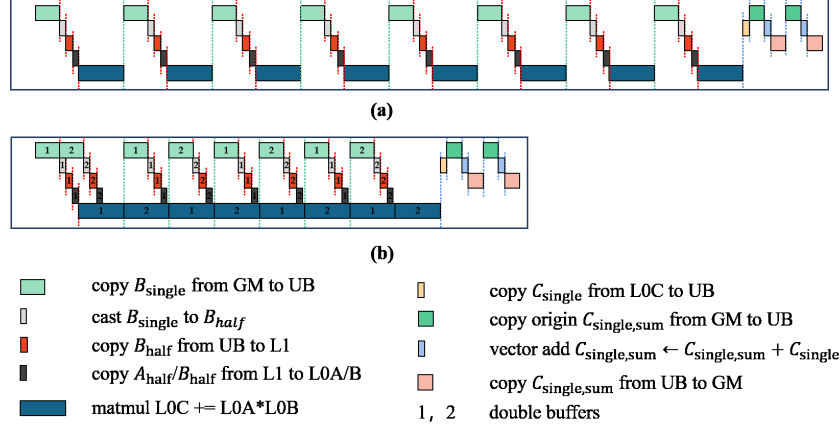


Figure 6: Comparison of single- and double-buffered pipelines based on L1 reuse

#### 4. Experimental Results

Experiments are conducted primarily on the Ascend 910A platform to evaluate the numerical accuracy and performance of the proposed method. For error comparison, OpenBLAS SGEMM is executed on a 192-core Kunpeng ARM CPU, while both HGEMM and H2SGEMM are run on the Ascend 910A NPU. Additionally, SGEMM from the CANN library is benchmarked on the newer Ascend 910B3 platform. Performance evaluation is also performed on both 910A and 910B3, including H2SGEMM on 910A and CANN SGEMM on 910B3. The hardware configurations are as follows:

- 910A platform:** Equipped with a 192-core 64-bit Kunpeng 920 ARM CPU across 4 sockets (48 cores per socket), organized into 8 NUMA nodes. Each core has 64 KB L1 cache, 512 KB L2 cache, and 48 MB shared L3 cache. The Ascend 910A NPU features 32 AI cores with a 1 GHz clock, 1.2 TB/s bandwidth, and no native FP32 matrix units. H2SGEMM runs on this platform. Further architectural details are shown in Fig. 3.
- 910B3 platform:** Features 20 AI cores operating at 1.8 GHz, with half the L1 buffer size of 910A, but twice the main memory capacity and a memory bandwidth of 1.6 TB/s. It supports native FP32 GEMM with a theoretical peak of 73.73 TFLOPs.



---

**Algorithm 1** Double-buffered GEMM pipeline for  $R_{A,\text{half}} \times B$ 

---

**Input:**  $R_{A,\text{half}}$  partitioned into  $M \times K$  blocks,  $B$  into  $K \times N$

**Main Loop:** Compute  $R_{A,\text{half}} \times B$

```
1: for each block row of  $R_{A,\text{half}}$  (parallel over  $N_{\text{core}}$  cores) do
2:   for each group ( $G = K/N_{\text{fused}}$  total) do
3:     for each of the  $N_{\text{fused}}$  blocks in the group do
4:        $A_{\text{single}}$ : GM  $\rightarrow$  UB
5:        $A_{\text{single}} \Rightarrow A_{\text{half}} \Rightarrow \text{to\_single}(A_{\text{half}})$ : VEC
6:        $(A_{\text{single}} - \text{to\_single}(A_{\text{half}})) \times sf \Rightarrow R_{A,\text{single}} \Rightarrow R_{A,\text{half}}$ : VEC
7:        $R_{A,\text{half}}$ : UB  $\rightarrow$  L1
8:     end for
9:     for each column block of matrix  $B$  do
10:      for  $N_{\text{fused}}$  blocks with double-buffering in L1 do
11:         $B_{\text{single}}$ : GM  $\rightarrow$  UB
12:         $B_{\text{single}} \Rightarrow B_{\text{half}}$ : VEC
13:         $B_{\text{half}}$ : UB  $\rightarrow$  L1  $\rightarrow$  L0B
14:         $R_{A,\text{half}}$ : L1  $\rightarrow$  L0A
15:         $R_{A,\text{half}} \times B_{\text{half}} + C_{\text{single}} \Rightarrow C_{\text{single}}$ : CUBE
16:      end for
17:       $C_{\text{single}}$ : L0C  $\rightarrow$  UB
18:      for each block of  $C_{\text{single}}$  (split if UB is insufficient) do
19:         $C_{\text{single,sum}}$ : GM  $\rightarrow$  UB
20:         $C_{\text{single,sum}} + C_{\text{single}} \Rightarrow C_{\text{single,sum}}$ : VEC
21:         $C_{\text{single,sum}}$ : UB  $\rightarrow$  GM
22:      end for
23:    end for
24:  end for
25: end for
```

**Output:** Final output  $R_{A,\text{half}} \times B$

---

#### 4.1. Relative Error Evaluation

To investigate the numerical behavior of Eq. 7, we assess the influence of accumulation order on relative error. Fig. 7(a) shows the element-wise evaluation approach, where all three terms of  $C_{\text{single}}$  are computed and summed per position. Due to the much smaller magnitude of  $R_{A,\text{half}}$  and  $R_{B,\text{half}}$  compared to  $A_{\text{half}}$  and  $B_{\text{half}}$ , this approach is more susceptible to rounding and underflow errors.

In contrast, Fig. 7(b) shows the term-wise evaluation strategy, which first computes the three component matrices of  $C_{\text{single}}$  independently and then sums them. This separation reduces rounding error propagation and underflow risk, making term-wise computation more suitable for precision-

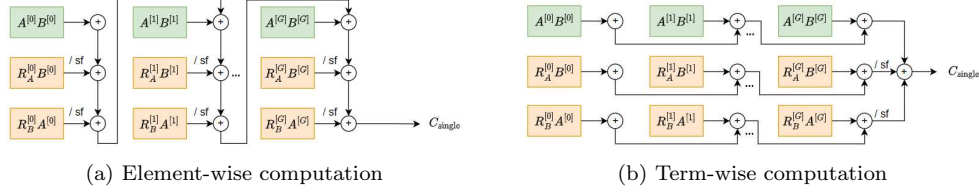


Figure 7: Computation sequences of the H2SGEMM precision compensation algorithm

critical applications.

The relative error is defined as:

$$\text{err} = \frac{\|C_{\text{true}} - C_{\text{calculated}}\|_2}{\|C_{\text{true}}\|_2} \quad (11)$$

Here,  $\|\cdot\|_2$  denotes the L2 norm. The ground-truth result  $C_{\text{true}}$  is computed using FP64 DGEMM on either the Kunpeng CPU or the Ascend 910B3 NPU. The calculated result  $C_{\text{calculated}}$  includes those from H2SGEMM (both element-wise and term-wise variants) and OpenBLAS SGEMM (FP32).

Fig. 8 shows the relationship between relative error and the offset exponent of FP32 inputs under uniform sampling. In Fig. 8(a), input matrices are sampled uniformly from the range  $[-2^{\text{offset exponent}}, 2^{\text{offset exponent}}]$ , resulting in a mean of zero. In contrast, Fig. 8(b) uses non-negative sampling from  $[0, 2^{\text{offset exponent}}]$ .

We focus on non-positive offset exponents to probe error amplification in underflow-prone regions. Smaller offset exponents correspond to values closer to zero and are more likely to trigger underflow, making them ideal for studying numerical robustness. Furthermore, in Fig. 8(a), since the input matrices contain both positive and negative values, destructive cancellation during matrix multiplication can significantly reduce the magnitude of the output matrix  $C_{\text{true}}$ . As the L2 norm of  $C_{\text{true}}$  appears in the denominator of the relative error definition (Eq. 11), this reduction amplifies the computed relative error. This effect is absent in Fig. 8(b), making the two settings complementary.

Results show that vanilla half-precision GEMM yields the largest relative error ( $10^{-4}$ ), making it unsuitable for high-accuracy applications such as deep neural network layers or scientific computing with many iterations. In contrast, H2SGEMM significantly improves accuracy.

Without scaling, term-wise and element-wise variants of H2SGEMM exhibit similar error, though the former is slightly better near offset exponent 0.

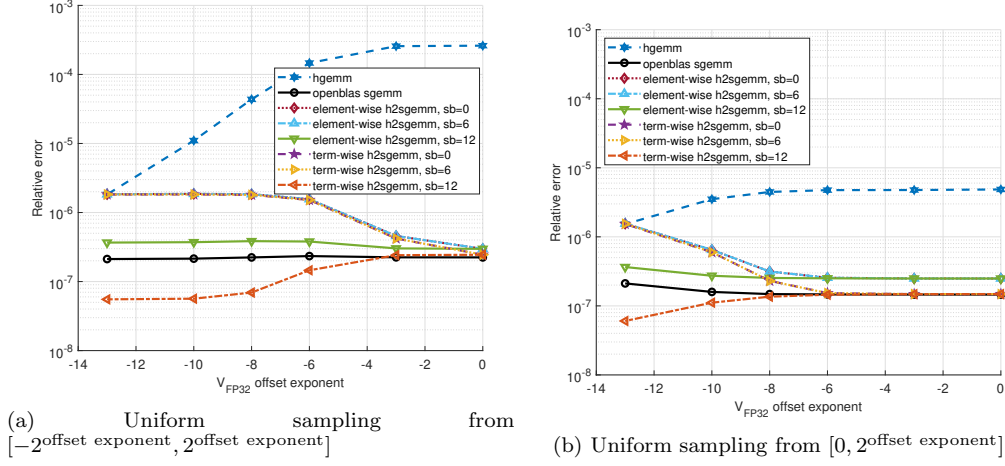


Figure 8: Relative error vs. offset exponent under different input ranges

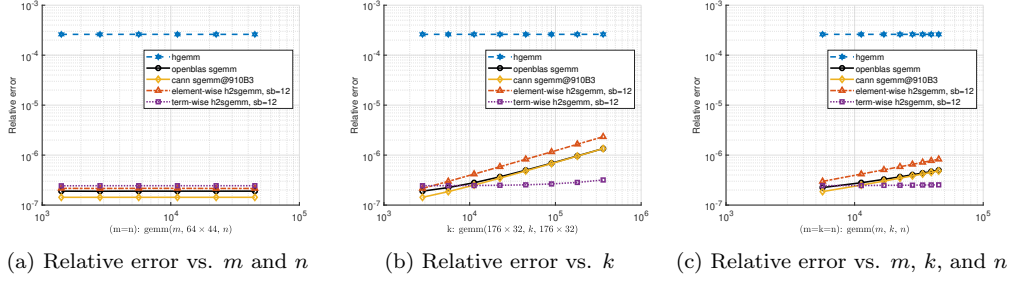


Figure 9: Relative error vs. input matrix sizes

However, both have higher error than SGEMM, highlighting that precision recovery in H2SGEMM critically depends on low-part amplification. Applying  $sb = 12$  yields  $1 \sim 2$  orders of magnitude error reduction, particularly in low-exponent regions. In comparison,  $sb = 6$  performs poorly, validating the scaling theory in Section 3.1.3.

With  $sb = 12$ , element-wise H2SGEMM achieves accuracy comparable to SGEMM, while term-wise H2SGEMM surpasses SGEMM in small-exponent regions. This improvement stems from its accumulation strategy, where smaller-magnitude terms are summed first, followed by larger-magnitude terms, thereby minimizing rounding errors through better numerical stability.

Fig. 9 explores how relative error scales with matrix dimensions under fixed exponent (offset exponent = 0). In Fig. 9 (a),  $m$  and  $n$  are varied while

$k$  is fixed at  $64 \times 44$ , matching the optimal blocking and fusion settings in Section 4.2. In Fig. 9 (b),  $k$  is varied while  $m = 176$ ,  $n = 32$  (matching optimal block size  $\times$  core count). In Fig. 9 (c), all three dimensions are varied.

Errors are stable across  $m, n$  (Fig. 9a), since accumulation depth is unchanged. However, as  $k$  increases (Fig. 9b, c), term-wise H2SGEMM scales better than SGEMM or other variants, maintaining lower error due to more robust accumulation. This highlights its suitability for large-scale high-precision applications. Due to space limitations, we do not provide detailed analysis for other cases with smaller offset exponents. However, the observed trends are consistent with the results presented in Fig. 9, and are therefore omitted.

#### 4.2. Performance Evaluation

Fig. 10 evaluates how matrix block size and pipeline strategy affect H2SGEMM throughput on Ascend 910A. In Fig. 10 (a), the single-buffered pipeline peaks at 41.7 TFLOPs, while (b) shows that the double-buffered version reaches 65.3 TFLOPs—a 57% gain—by reducing data transfer latency and contention. This achieves 77% of the theoretical FP32-equivalent peak of Ascend 910A ( $256 \text{ TFLOPs} / 3 = 85.3 \text{ TFLOPs}$ ).

Low-performance points correspond to small block sizes, which suffer from poor L0A/L0B utilization, as these were not constrained in Eq. 10. Overall, performance is highly sensitive to blocking parameters. With an optimal configuration of  $(b_m, b_k, b_n, N_{\text{fused}}) = (176, 64, 176, 44)$ , the double-buffered pipeline achieves maximum throughput.

Fig. 11 explores performance scaling with matrix size. In Fig. 11 (a), increasing  $m$  and  $n$  steadily improves H2SGEMM throughput, reaching over 60 TFLOPs, slightly outperforming SGEMM from CANN on Ascend 910B3. In Fig. 11 (b), as  $k$  increases, performance of both H2SGEMM and CANN SGEMM remains steady, with H2SGEMM on 910A reaching 60 TFLOPs, close to the 63 TFLOPs on 910B3. Despite lacking native FP32 units, H2SGEMM delivers near-peak performance on 910A. In Fig. 11 (c), where all dimensions grow, CANN SGEMM suffers from performance drop-off, while H2SGEMM remains stable and eventually surpasses it, demonstrating better scalability and robustness.

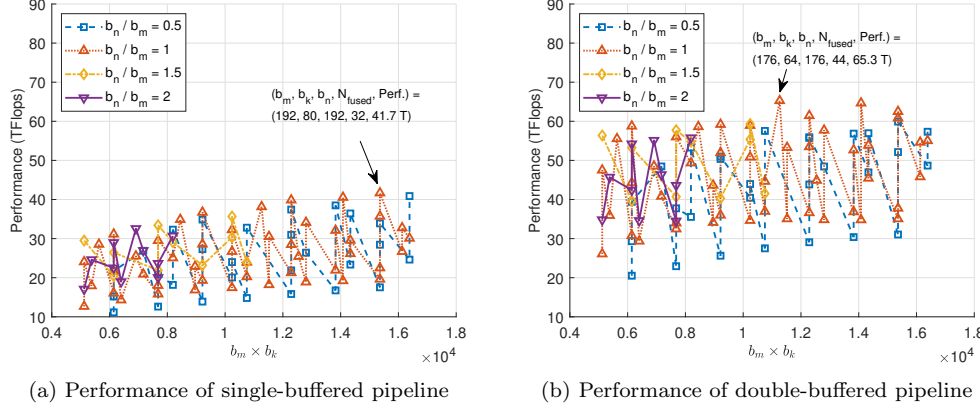


Figure 10: Performance impact of matrix blocking with L1 cache reuse

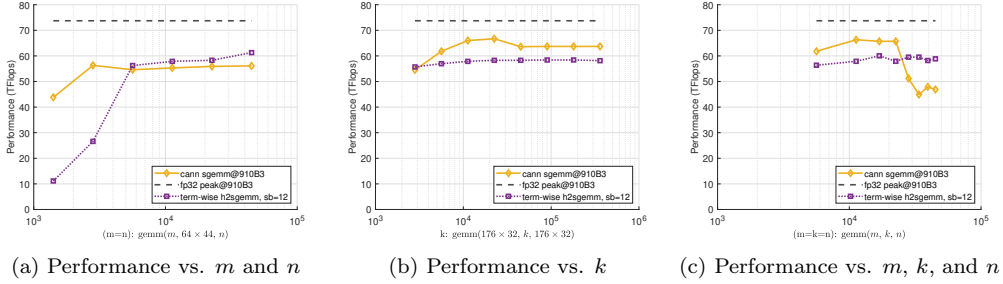


Figure 11: Performance vs. input matrix sizes

## 5. Conclusion

We present H2SGEMM, a high-performance algorithm for FP32 GEMM on low-precision hardware. By combining FP16 decomposition, numerical error control, computation order tuning, and cache-aware execution, H2SGEMM bridges the gap between accuracy and throughput. This enables efficient execution of full-precision workloads on emerging AI processors lacking high precision compute units.

## References

- [1] H. Yu, H. Li, H. Shi, T. S. Huang, G. Hua, Any-precision deep neural networks, in: Proceedings of the AAAI Conference on Artificial Intelligence, Vol. 35, 2021, pp. 10763–10771.

- [2] B. Zhuang, L. Liu, M. Tan, C. Shen, I. Reid, Training quantized neural networks with a full-precision auxiliary module, in: Proceedings of the IEEE/CVF conference on computer vision and pattern recognition, 2020, pp. 1488–1497.
- [3] A. Vansteenkiste, J. Leliaert, M. Dvornik, M. Helsen, F. Garcia-Sanchez, B. Van Waeyenberge, The design and verification of mumax3, *AIP advances* 4 (10) (2014).
- [4] G. P. Müller, M. Hoffmann, C. Dißelkamp, D. Schürhoff, S. Mavros, M. Sallermann, N. S. Kiselev, H. Jónsson, S. Blügel, Spirit: Multifunctional framework for atomistic spin simulations, *Physical review b* 99 (22) (2019) 224414.
- [5] B. D. Wozniak, F. D. Witherden, F. P. Russell, P. E. Vincent, P. H. Kelly, Gimmik—generating bespoke matrix multiplication kernels for accelerators: Application to high-order computational fluid dynamics, *Computer Physics Communications* 202 (2016) 12–22.
- [6] M. Cawkwell, E. Sanville, S. Mniszewski, A. M. Niklasson, Computing the density matrix in electronic structure theory on graphics processing units, *Journal of chemical theory and computation* 8 (11) (2012) 4094–4101.
- [7] H. Liao, J. Tu, J. Xia, H. Liu, X. Zhou, H. Yuan, Y. Hu, Ascend: a scalable and unified architecture for ubiquitous deep neural network computing: Industry track paper, in: 2021 IEEE International Symposium on High-Performance Computer Architecture (HPCA), IEEE, 2021, pp. 789–801.
- [8] K. Ozaki, T. Ogita, S. Oishi, S. M. Rump, Error-free transformations of matrix multiplication by using fast routines of matrix multiplication and its applications, *Numerical Algorithms* 59 (2012) 95–118.
- [9] S. Markidis, S. W. Der Chien, E. Laure, I. B. Peng, J. S. Vetter, Nvidia tensor core programmability, performance & precision, in: 2018 IEEE international parallel and distributed processing symposium workshops (IPDPSW), IEEE, 2018, pp. 522–531.
- [10] B. Feng, Y. Wang, G. Chen, W. Zhang, Y. Xie, Y. Ding, Egemm-tc: accelerating scientific computing on tensor cores with extended precision,

- in: Proceedings of the 26th ACM SIGPLAN symposium on principles and practice of parallel programming, 2021, pp. 278–291.
- [11] H. Ootomo, R. Yokota, Recovering single precision accuracy from tensor cores while surpassing the fp32 theoretical peak performance, *The International Journal of High Performance Computing Applications* 36 (4) (2022) 475–491.
  - [12] M. Fasi, N. J. Higham, M. Mikaitis, S. Pranesh, Numerical behavior of nvidia tensor cores, *PeerJ Computer Science* 7 (2021) e330.
  - [13] Z. Ma, H. Wang, G. Feng, C. Zhang, L. Xie, J. He, S. Chen, J. Zhai, Efficiently emulating high-bitwidth computation with low-bitwidth hardware, in: Proceedings of the 36th ACM International Conference on Supercomputing, 2022, pp. 1–12.
  - [14] W. Kahan, Ieee standard 754 for binary floating-point arithmetic, *Lecture Notes on the Status of IEEE 754 (94720-1776)* (1996) 11.
  - [15] W. Xue, K. Yang, Y. Liu, D. Fan, P. Xu, Y. Tian, Unlocking high performance with low-bit npus and cpus for highly optimized hpl-mxp on cloud brain ii, in: SC24: International Conference for High Performance Computing, Networking, Storage and Analysis, IEEE, 2024, pp. 1–16.